Current Research in Green and Sustainable Chemistry 4 (2021) 100156

Contents lists available at ScienceDirect

Current Research in Green and Sustainable Chemistry

journal homepage: www.elsevier.com/journals/current-research-in-green-and-sustainable-chemistry/2666-0865

Fabrication of Fe_2TiO_5/TiO_2 binary nanocomposite from natural ilmenite and their photocatalytic activity under solar energy

Charitha Thambiliyagodage [a,*], Shanitha Mirihana [a], Ramanee Wijesekera [b], Dinu Sri Madusanka [c], Murthi Kandanapitiye [c], Martin Bakker [d]

[a] School of Science and Education, Faculty of Humanities and Sciences, Sri Lanka Institute of Information Technology, New Kandy Road, Malabe, Sri Lanka
[b] Department of Chemistry, Faculty of Science, University of Colombo, Colombo 3, Sri Lanka
[c] Department of Nano Science Technology, Wayamba University of Sri Lanka, Kuliyapitiya, Sri Lanka
[d] Department of Chemistry and Biochemistry, The University of Alabama, Tuscaloosa, AL, 35387-0336, USA

ARTICLE INFO

Keywords:
Ilmenite
Pseudobrookite
Photocatalysis
Solar energy

ABSTRACT

Heterogeneous photocatalysis is an attractive alternative route to enhance the degradation of environmental pollutants. In this work, we have fabricated Fe_2TiO_5/TiO_2 binary nanocomposites using natural ilmenite *via* bottom up approach. Synthesized nanocomposites were characterized by X-ray diffractometry, X-ray fluorescence, transmission electron microscopy, Raman spectroscopy, diffuse reflectance UV–Visible spectroscopy, scanning electron microscopy, and X-ray photoelectron spectroscopy. These nanoparticles are in the range of 40–70 nm and are of type I heterostructure with a band gap of 2.02 eV. They are sensitive to visible light and show higher photocatalytic activity under direct solar energy. Photocatalytic activity of Fe_2TiO_5/TiO_2 was assessed using a model textile dye, methylene blue. Over a period of 2 h, 76% of methylene blue was photodegraded at a rate of 0.0084 min^{-1} in the presence of Fe_2TiO_5/TiO_2.

1. Introduction

Finding practical techniques to producing a clean environment is a globally demanding challenge. Environmental pollution caused by anthropogenic activities such as development of industries and agriculture has resulted in the release of heavy metals [1], textile dyes [2], pesticides [3], fertilizers [4], pharmaceuticals [5] to water reservoirs. Such contaminants cause adverse effects to all living beings including human beings [6]. There are many existing methods to purify wastewater such as chemical precipitation [7], adsorption [8], filtration [9], ion exchange [10], oxidation [11], and electrolysis [12]. However, alternative methods are being sought because the current methods are expensive, have limited selectivity and materials used have a short life time. Advanced oxidation process (AOP) is an alternative pollutant destructive technology which can completely degrade organic molecules to harmless CO_2 and H_2O. AOP is characterized by its ability of exploit the high reactivity of hydroxyl radicals (oxidation potential 2.8 V) to mineralize the organic pollutants [13]. Various semiconductor materials have been used as photocatalysts including TiO_2 nanoparticles [14], ZnO [15], iron oxide nanostructures [16] etc and among them TiO_2 has been the most studied due to its ability to cause complete mineralization. However, the most stable oxides such as TiO_2 and ZnO are sensitive to only ultraviolet light limiting their application in visible light. Although some semiconductors such as Fe_2O_3 were reported to be able to absorb visible light, their photocarrier utilization and quantum efficiency are comparatively low [17,18]. TiO_2 has been doped with metals like Fe [19], Cu [20], Pt [21] and nonmetals including N [22], C [23] and S [24] to increase its visible light sensitivity. Interestingly, the scope of using AOP has broaden to explore alternatives. Researchers have focused on synthesizing nanocomposites such as $CuWO_4/CuO$ [25], $VO_x/g\text{-}C_3N_4$ [26], $Ag_3PO_4/P\text{-}g\text{-}C_3N_4$ [27], Co–Fe bimetallic based metal-organic frame works [28], bimetallic Ag/Pt nanoparticles [29] etc. as efficient photocatalysts for photodegradation of dyes [25,26], antibacterial activity [25,28,29], H_2 production [27], pharmaceutical degradation [28] due to excellent charge separation. Novel nanohybrids such as $CaIn_2S_4/WS_2$ [30], $Cu_2In_2ZnS_5/Gd_2O_2S$:Tb [31], $ZnIn_2S_4$/UiO-66 [32], $MoSe_2$/ZnO/ZnSe [33] have shown phtocatalytic activity for Cr(VI) reduction due to enhanced charge separation by inhibition of the recombination of photogenerated electrons and holes. Composites such as Al_2O_3–Cr_2O_3 [34], WSi_2/W [35] and $MoSi_2$ and $Si/MoSi_2$ coated TZM

* Corresponding author.
E-mail address: charitha.t@sliit.lk (C. Thambiliyagodage).

https://doi.org/10.1016/j.crgsc.2021.100156
Received 21 May 2021; Received in revised form 20 July 2021; Accepted 22 July 2021
Available online 24 July 2021

(Mo-0.5Ti-0.1Zr-0.02C) alloy [36] have shown excellent mechanical properties. It is highly desirable yet challenging to find effective semiconductor materials that are capable of using the abundant solar light.

Extensive deposits of ilmenite which are also rich in rutile and zircon could be found in sea beaches in areas such as Pulmodai and Induwara, Sri Lanka. Ilmenite could be used as a source of Ti in various Ti based applications such as Ti based pigment in house paints, plastics, and paper [37]. Ti alloys are used in aircrafts due to their low density, high strength and ability to withstand high temperatures. Ti is used in power plant condensers due to its high resistance to corrosion [38]. The main disadvantage associated with the deposits is that ilmenite sand cannot be applied directly to the above industries due to its macro nature, resulting in low effectiveness efficiency. Special properties associated with nanomaterials are large surface to volume ratio and increased surface activity compared to the bulk material. Hence, control of particle size and morphology play a crucial role in activity related applications [39]. Therefore, reducing the particle size and modifying the morphology accordingly, are important factors in improving the activity of naturally available ilmenite. Scientists worldwide have researched on techniques that could be used to modify ilmenite prior subjecting to many advanced applications including oxidation and reduction [40–42]. In the light of the aforementioned requirements we synthesized Fe_2TiO_5/TiO_2 nanocomposites using ilmenite sand as the raw material by a simple chemical method involving both top down and bottom up approaches. Fe_2TiO_5 is a narrow band gap (~2.2 eV) semiconductor, and hence could be used as a photocatalyst in visible light for water splitting to generate an alternative energy source [43,44]. Moreover, Fe_2TiO_5 can be applied in various applications such as, as an anode in Li-ion batteries [45], in the catalytic reduction of NO with NH_3 [46], in proton exchange membrane fuel cells as a dispersion in the Nafion membrane to improve the water uptake, in proton conductivity and in improving thermal stability [47] etc. Heterostructure Fe_2TiO_5/TiO_2 nanoparticles have been shown to be effective in degradation of dyes such as Rhodamine B [39,48] methylene blue (MB) [39] and for water oxidation [44] etc. upon visible light exposure. Fe_2TiO_5/TiO_2 has been synthesized using different expensive and hazardous chemicals such as titanium (IV) isopropoxide [39], titanium foil [44], tetra butryl titanate [48] as the titanium source, $Fe(NO_3)_3$ as the iron source with other chemicals such as oleic acid, oleylamine, CTAB, SDS [39], ethylene glycol, NH_4F [44] etc. by different techniques including electrochemical deposition [44]. Here we report the synthesis of nanoheterostructures *via* a simple chemical method using natural ilmenite as the only titanium and iron source and its photocatalytic activity in degradation of a textile dye, methylene blue. to We also believe that it would be an ideal way to add value to naturally available raw materials that could lead to commercialization. Further, the decontamination process would be eco-friendly as water purification by removing the textile dye, methylene blue could be achieved by a phtocatalyst synthesized by naturally available material.

2. Materials and methods

All chemicals were obtained commercially and used without further purification. Ilmenite sand was supplied by Lanka Mineral Sands Limited. HCl (37.5%), Methylene Blue and NH_3 (28%) were purchased from Daejung Chemical & Metal Co., Ltd. AgCl (99%) was procured from Himedia Leading Biosciences company. Deionized water (DI), with resistivity greater than 18.0 MΩ cm (Millipore Milli-Q system) was used. Ilmenite sand was washed with distilled water until the washings were clear followed by ethanol to remove any impurities present, and dried at 100 °C for 24 h. Purified ilmenite sand (2 g) was reacted with conc. HCl acid (50 ml) in a refluxing apparatus at 80 °C for 3 h and was incubated in the same acid for 24 h at room temperature. The liquid portion was collected and another 50 ml of conc. HCl was introduced to this partially digested ilmenite sand. The refluxing procedure was performed four times to ensure maximum digestion of ilmenite sand. To the combined liquid portions, dilute H_2SO_4 was added at 60 °C and stirring was continued until no fumes (presumably HCl) were observed. Conc. NH_3 was added dropwise to the stirring mixture until the pH reached 8. The resulting brown colour precipitate was stirred overnight and washed with DI water until the washings were negative for Cl^- ions (AgCl test). Precipitate was dried and calcined at 800 °C for 2 h in a muffle furnace.

The photocatalytic activity of the synthesized Fe_2TiO_5/TiO_2 nanocomposites in degradation of methylene blue was assessed under natural sunlight. Intensity of sunlight was in the range of 80,000–1200000 lux during the experiments. Catalyst (0.2 g) was added to 100 ml of 3 mg/L MB solution and the samples were kept in the dark to reach the adsorption-desorption equilibrium. Aliquots (~3 ml) were withdrawn at 15 min intervals for 2 h and centrifuged at 6000 rpm. The progress of the photocatalytic performance was monitored by UV–Visible spectrophotometry by scanning the absorbance of each sample in the range 200–800 nm.

3. Characterization

X-ray diffraction (XRD) analysis was carried out using an Advance Bruker system using CuKα (λ = 0.154 nm) radiation and 2θ varying from 5° to 80° at a scan speed of 2°/min. The chemical composition of the samples was analyzed by X-ray fluorescence (XRF) using a HORIBA Scientific XGT -5200 X-ray analytical microscope equipped with a Rh anode X-ray tube operated at a maximum voltage of 50 kV. The morphology of the samples was observed by a High Resolution Transmission Electron Microscope operating at 200 kV (JEOL - JEM – 2100) and energy dispersive spectra (EDS) were collected by the same instrument with TEAM EDX software. The sample (1 μl) was mounted on a holey carbon copper grid and allowed to dry at room temperature prior to TEM analysis. SEM images and EDS spectra were collected by Hitachi SU6600 Analytical Variable Pressure FE-SEM (Field Emission Scanning Electron Microscope) and Oxford Instruments EDX with AZtec software. Samples were mounted onto the sample stub using carbon tapes and the images were taken after gold sputter coating for 15 s. XPS spectra were acquired by Thermo Scientific™ ESCALAB Xi $^+$ X-ray Photoelectron Spectrometer. Shimadzu 1800 UV/Visible spectrophotometer utilizing a precision Czerny-Turner optical system was used to analyse diffuse reflectance spectra of the prepared powder samples. The measurements were carried out through the range of 190–1100 nm with a bandwidth of 1.0 nm (wavelength accuracy + - 0.1 nm). Absorbance of MB samples was measured by a Shimadzu UV-1990 double beam UV–Visible spectrophotometer. Raman analysis was performed by a Bruker Senterra Raman microscope spectrophotometer.

4. Results and discussion

4.1. Synthesis of the nanocomposites

The following reaction mechanism could be suggested for the synthesis of binary nanocomposites from natural ilmenite sand.

Reaction of Ilmenite, $FeTiO_3$ with conc. HCl,

Ilmenite when treated with concentrated HCl, produces a mixture of $TiOCl_2$ and $FeCl_2$ as a yellow colour solution as shown in equation (1) and (2). The overall reaction could be written as shown in equation (3) [49].

$$FeO + 2HCl = FeCl_2 + H_2O \quad (1)$$

$$TiO_2 + 2\ HCl = TiOCl_2 + H_2O \quad (2)$$

$$FeTiO_3 + 4HCl = FeCl_2 + TiOCl_2 + 2H_2O \quad (3)$$

Once diluted H_2SO_4 is added, $TiOCl_2$ and $FeCl_2$ hydrolyze producing HCl that eliminates from the reaction mixture as a gas as represented in equation (4) and (5) [50].

$$TiOCl_2 + H_2SO_4 = TiO\text{–}SO_4 + 2\ HCl \quad (4)$$

$$FeCl_2 + H_2SO_4 = FeSO_4 + 2\ HCl \quad (5)$$

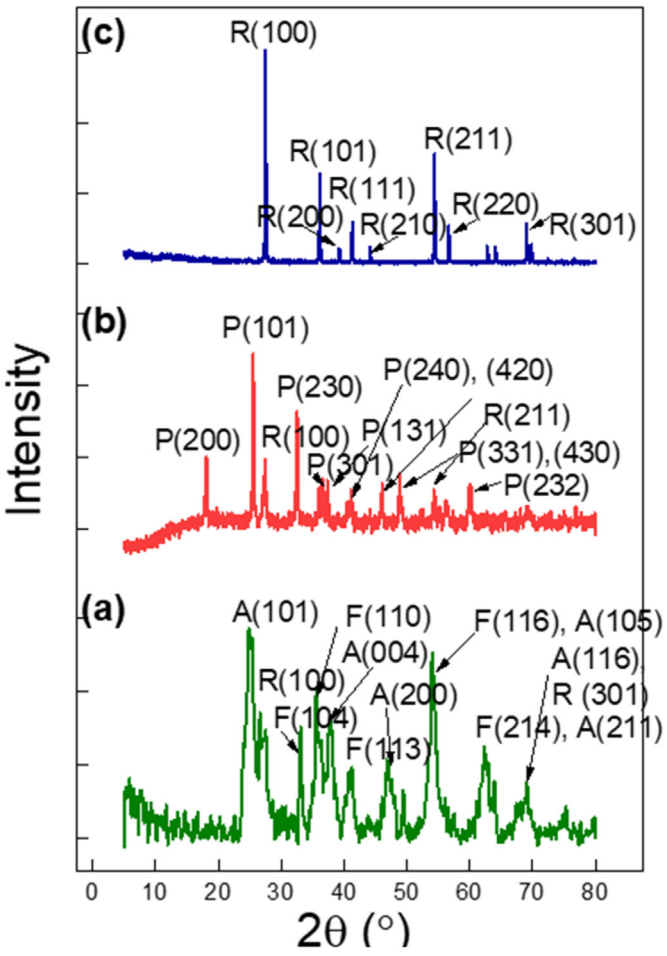

Fig. 1. XRD patterns of (a) nanocomposite before calcination, (b) nanocomposite after calcination (b) TiO_2.

When conc. NH_3 is added to the resulting mixture a brown coloured precipitate forms as given in equation (6)–(10) [50]. During annealing, the crystal structure of Fe_2TiO_5 develops (equation (11)) [51].

$$TiO–SO_4 + 2\ NH_3{\cdot}H_2O = H_2TiO_3 + (NH_4)_2SO_4 \quad (6)$$

$$H_2TiO_3 = TiO_2 + H_2O \quad (7)$$

$$FeSO_4 + 2\ NH_4OH = Fe(OH)_2 + (NH_4)_2SO_4 \quad (8)$$

$$2H_2O + 2\ Fe(OH)_2 + O_2 = 2\ Fe(OH)_3 + H_2O_2 \quad (9)$$

$$2\ Fe(OH)_3 = Fe_2O_3 + 3H_2O \quad (10)$$

$$Fe_2O_3 + TiO_2 = Fe_2TiO_5 \quad (11)$$

The above proposed reaction mechanism is further supported by the XRD analysis discussed in section 4.2.

4.2. XRD analysis

The crystalline structure and the phase purity of the prepared nanocomposites were determined by XRD. The XRD pattern of the nanocomposite before calcination shows less intense peaks with a high signal-noise ratio. Peaks at 25.00°, 37.85°, 47.00° represent the (101), (004), and (200) planes of anatase phase (ICDD DB card No. 01-077-044) while the peak at 27° depicts the (100) plane of rutile phase. The peak at 69.10° shows the presence of both (116) plane of anatase and (301) of rutile phase. Peaks at 33.00°, 35.70°, 41.15° exhibit the (104), (110), and (113) planes of α-Fe_2O_3 (ICDD DB card No. 01-073-0603. Further, the peak at 54.00° represents the (116) plane of α-Fe_2O_3 and (105) plane of anatase, while the peak at 62.30° represents the (214) plane of α-Fe_2O_3 and (211) plane of anatase. The XRD pattern of the nanocomposites after the calcination is shown in Fig. 1 (b). The diffraction peaks at 2θ, 18.08°, 25.54°, 32.52°, 36.54°, 37.34°, 40.58°, 41.06°, 46.06°, 48.86°, 55.10°, 56.20°, 60.06° could be indexed to the (200), (101), (230), (301), (131), (240), (420), (331), (430), (060), (521), and (232) planes of the orthorhombic phase of Fe_2TiO_5 (pseudobrookite) (ICSD 35244). The calculated d spacings of 0.490, 0.349, 0.275, 0.248, 0.222, 0.219, 0.197, 0.187, 0.166 and 0.154 nm were in good agreement with the ICSD reference (a_o = 9.779 Å,b_0 = 9.978 Å,c_o = 3.739 Å). Other peaks at 27.40° (d = 0.325 nm) and 54.32° (0.168 nm) could be attributed to the (110) and (211) planes of the Rutile phase. XRD pattern of pure TiO_2 annealed at 800 °C is given in Fig. 1 (c) clearly shows the characteristic XRD pattern of the Rutile phase synthesized via sol gel synthesis method using Titanium isopropoxide as the precursor.

Crystallite sizes of Fe_2TiO_5 and TiO_2 were calculated to be 39.8 nm and 30.3 nm, respectively using the main diffraction peaks at 25.54° and 27.40°. The weight fractions of the different phases of composite are estimated using the intensities of their main XRD diffraction peaks where I_P and I_R are the intensities of the main diffraction peaks of Fe_2TiO_5 and Rutile at 25.54° and 27.40°, respectively and K_P and K_R are the reference intensity ratio values of Fe_2TiO_5 and Rutile, respectively [52,53].

$$x_P = 1/(1+ K_P/ K_R.\ I_R/ I_P)$$

The calculated weight ratio of Fe_2TiO_5 to Rutile is 83:17 and the molar ratio is 66.3 : 40.7. Therefore, the synthesized sample has five times more Fe_2TiO_5 than Rutile. The acquired XRD patterns further confirm the proposed mechanism in 4.1 where before the calcination mainly α-Fe_2O_3 and TiO_2 (anatase) compounds have been formed with some TiO_2 (rutile) and upon calcination, at 800 °C these compounds together have formed Fe_2TiO_5 and excess TiO_2 remains as TiO_2 (Rutile).

Table 1
Metal Oxide composition of ilmenite.

Material	Spot 1 Mass %	Spot 2 Mass %	Spot 3 Mass %	Spot 4 Mass %	Spot 5 Mass %	Spot 6 Mass %
MgO	6.14	-	-	-	-	-
Al_2O_3	4.37	1.81	0.05	0.23	0.77	0.04
SiO_2	13.04	3.48	2.95	1.34	1.40	1.47
P_2O_5	-	-	-	0.15	-	0.14
K_2O	0.48	-	-	-	-	-
CaO	3.35	0.08	0.27	-	-	-
TiO_2	41.64	57.17	48.41	50.52	44.51	50.98
Cr_2O_3	0.09	0.22	0.08	0.22	0.10	0.22
MnO	0.64	0.53	0.89	0.59	2.03	0.59
Fe_2O_3	30.04	35.70	47.23	46.63	50.67	46.26
ZnO	-	0.08	-	0.19	0.03	0.18
ZrO_2	-	0.92	-	-	-	-

4.3. XRF analysis

Table 1 shows the XRF results of the ilmenite sand. Data were collected from six different spots of the sample. The major elemental

Table 2
Metal Oxide composition of Fe_2TiO_5/TiO_2

Material	Spot 1 Mass%	Spot 2 Mass%	Spot 3 Mass%	Spot 4 Mass%	Spot 5 Mass%	Spot 6 Mass%
Al_2O_3	0.65	-	0.55	0.57	0.50	0.61
SiO_2	0.26	0.89	0.92	0.88	1.00	0.94
P_2O_5	-	-	-	-	0.04	-
TiO_2	45.38	44.53	45.10	44.94	44.86	44.50
Cr_2O_3	0.11	0.10	0.10	0.21	0.11	0.11
MnO	0.23	0.20	0.21	-	0.21	0.24
Fe_2O_3	53.37	54.27	53.12	53.34	53.25	53.56
ZnO	-	-	-	-	0.03	0.04

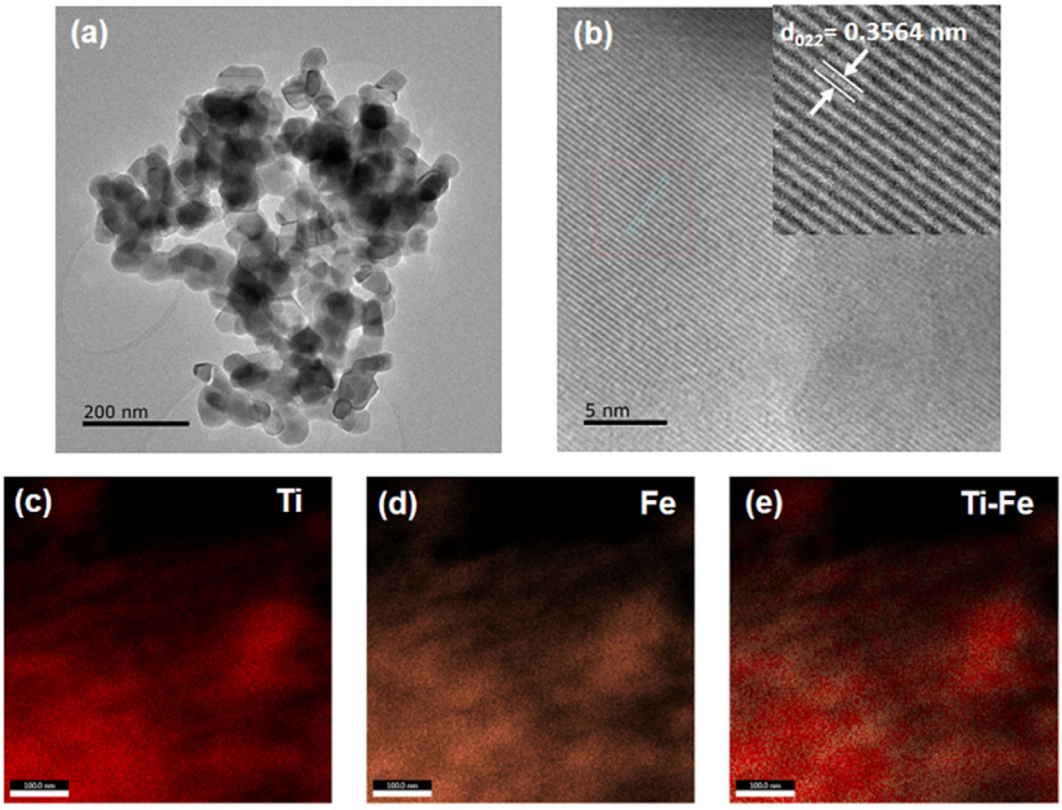

Fig. 2. (a) Bright field TEM image (b) HRTEM image of Fe_2TiO_5/TiO_2 nanocomposites, (c), (d), and (e) element maps indicating the presence and distribution of Ti, Fe and Ti–Fe, respectively.

composition in the sample were TiO_2, Fe_2O_3, SiO_2, MgO, and Al_2O_3 with mass percentage values of 48.87%, 42.76%, 3.95%, 6.14%, and 1.21%, respectively. In addition, MnO, ZrO_2, K_2O, P_2O_5, Cr_2O_3, ZnO are present in minor concentrations with mass percentage values of less than 1%. Mass percentages of all the elements are different from one spot to another indicating the heterogeneous distribution of elements. Elemental composition of the synthesized Fe_2TiO_5/TiO_2 nanocomposites analyzed by XRF is given in Table 2. TiO_2 and Fe_2O_3 are the major elemental species with an average mass percentages of 44.88% and 53.48%, respectively. All other species, SiO_2, Al_2O_3, P_2O_5, Cr_2O_3, MnO, ZnO are

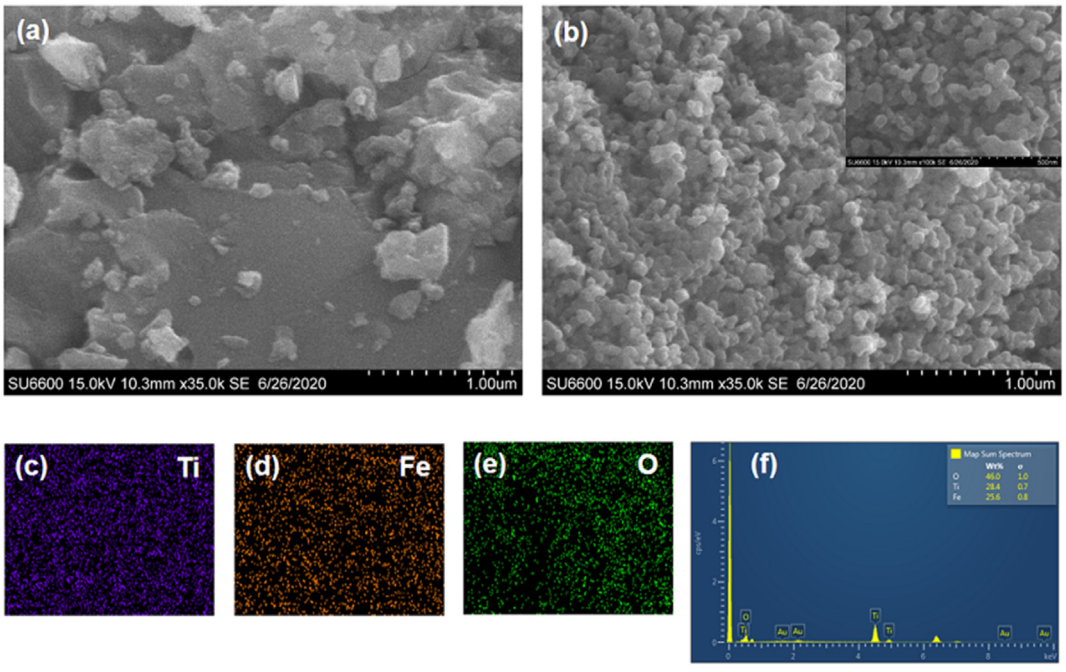

Fig. 3. SEM images of (a) natural ilmenite sand (b) Fe_2TiO_5/TiO_2 nanocomposites, (c), (d), (e) element maps of Ti, Fe, O, respectively, (f) EDS spectrum of Fe_2TiO_5/TiO_2 nanocomposites.

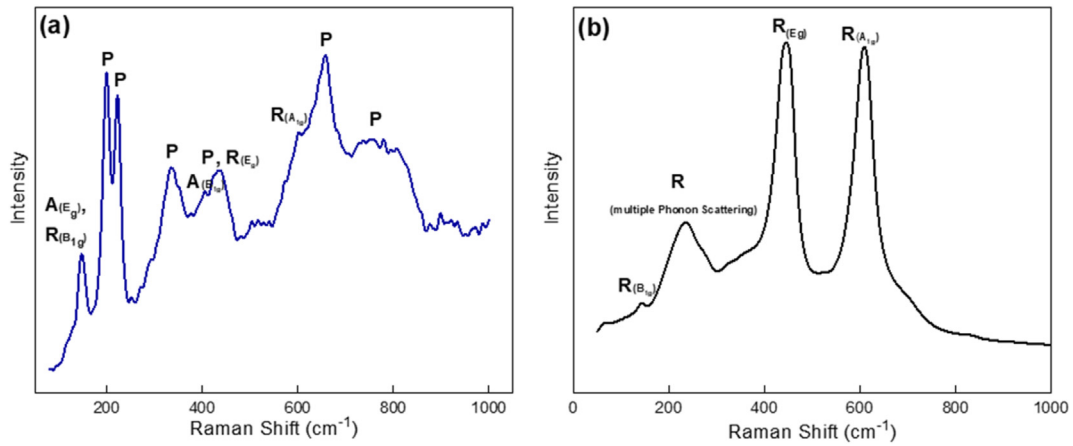

Fig. 4. Raman spectrum of (a) Fe_2TiO_5/TiO_2 nanocomposites (A-Anatase, R-Rutile, P- Pesudobrookite), (b) TiO_2.

present in concentrations less than 1%. SiO_2 and Al_2O_3 which were present as major constituents of ilmenite sand are present in low concentrations, on average 0.81 and 0.58%, respectively. This indicates that much of the SiO_2, Al_2O_3 and MgO impurities have been removed during the synthesis and washing procedures. Further, the composition of the synthesized nanocomposites show a relatively homogeneous distribution when the mass percentages of the analyzed six spots are considered.

4.4. TEM analysis

To gain insight on size, morphology and crystal structure of the synthesized nanostructures, TEM analysis was performed. The bright field TEM image shows (Fig. 2(a)) the nanoparticle distribution. Most of the nanoparticles are aggregated and irregular in shape, with some being spherical, pentagonal and hexagonal. Therefore, calculating the precise diameter of the nanoparticles is not meaningful. However, in general, the size of the nanoparticles was in the range of 40–70 nm. Comparison of the d spacing (0.3564 nm) obtained from the HRTEM image with that calculated using the XRD pattern (0.349 nm) of the prominent peak at 25.54° indicates that the atomic plane is the (101) plane of Fe_2TiO_5 (Fig. 2(b)). The slight difference in the d spacing values obtained by TEM and XRD could be attributed to the localized effect of TEM. According to the XRD data the ratio of Fe_2TiO_5 to TiO_2 is ~5:1. Hence, the atomic planes of TiO_2 could not be seen in the TEM images. The element maps of the individual elemental distribution of Ti and Fe are shown in Fig. 2(c) and (d), respectively and the composite of Fe–Ti in Fig. 2(e).

4.5. SEM analysis

SEM images were collected in order to study the morphology and the size of the synthesized nanocomposites. SEM image of ground natural ilmenite is shown in Fig. 3(a). It clearly shows the disorganized macro-nature of the sand particles. The SEM image of the synthesized nanoparticles (Fig. 3(b)) shows that nanoparticles are agglomerated and most of them are spherically shaped while some irregular shaped nanoparticles are also present. The insert of Fig. 3(b) shows a SEM image of

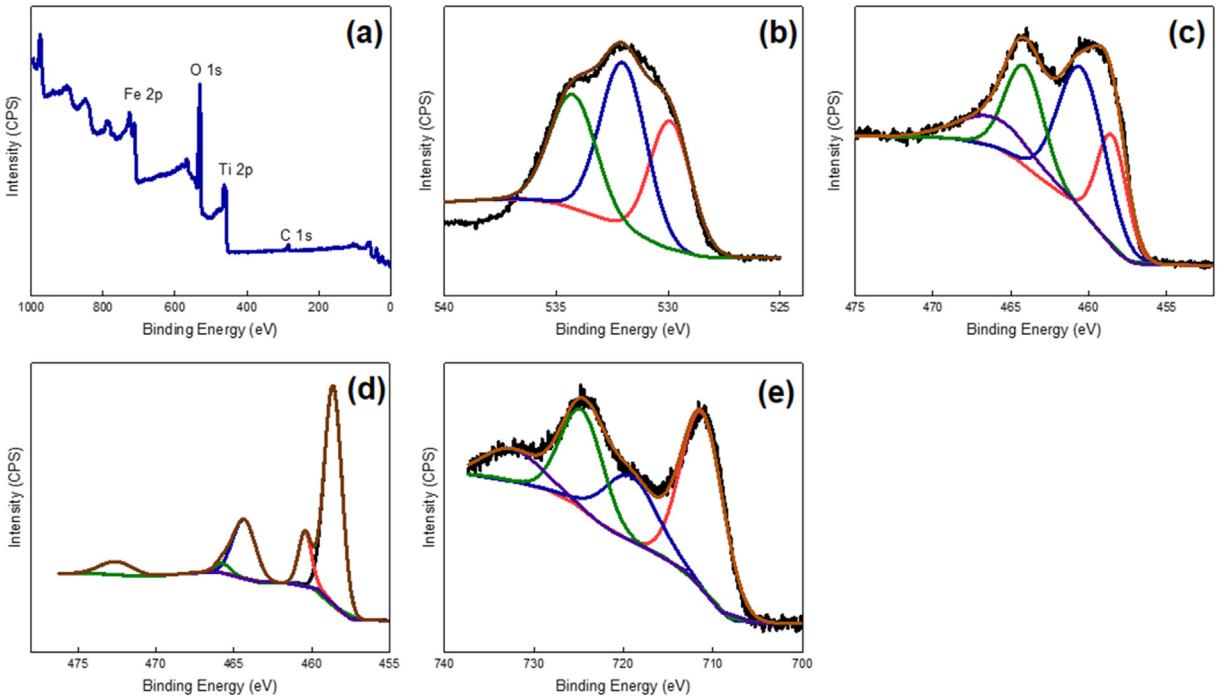

Fig. 5. (a) Survey spectrum, High resolution spectra of (b) O 1s, (c) Ti 2p (d) High resolution spectrum of Ti 2p of TiO_2 and (e) High resolution spectrum of Fe 2p of Fe_2TiO_5/TiO_2 nanocomposites.

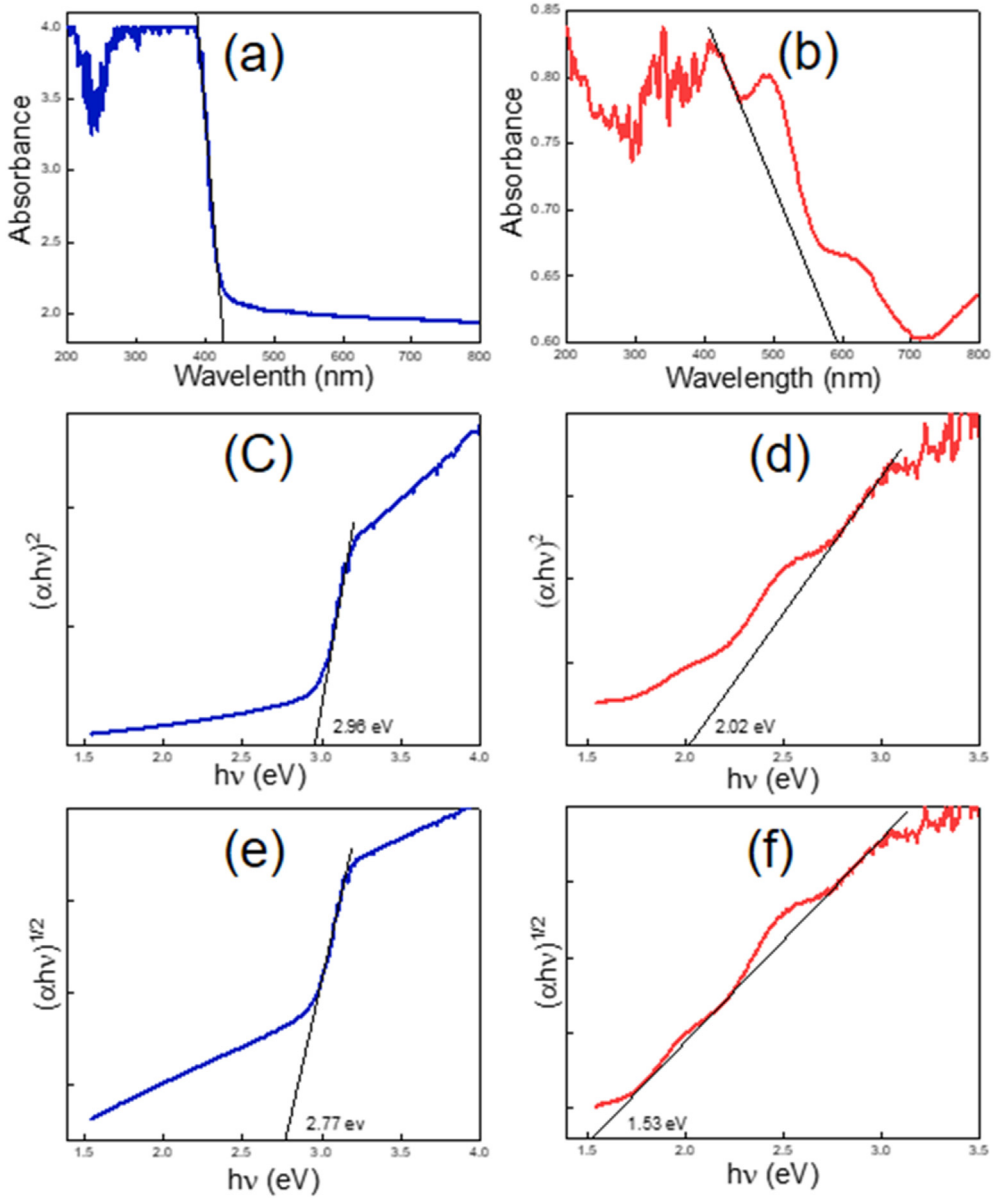

Fig. 6. UV–Vis DRS spectra of (a) TiO_2 (b) Fe_2TiO_5/TiO_2, plots of $(\alpha h\nu)^2$ versus photon energy ($h\nu$) for (c) TiO_2 (d) Fe_2TiO_5/TiO_2, plots of $(\alpha h\nu)^{1/2}$ versus photon energy ($h\nu$) for (e) TiO_2 (f) Fe_2TiO_5/TiO_2 E_{CB} and E_{VB} represent the band edge potentials of the conduction band (CB) and valence band (VB), respectively. These can be calculated from the following equations [67,70].

high magnification which gives a clear view of the shape and distribution of the nanoparticles. EDS element maps of Ti, Fe and O are given in Fig. 3(c), (d) and (e), respectively. They show that these elements are uniformly distributed in the matrix. Fig. 3(f) indicates the EDS spectrum of the synthesized nanoparticles in the microscale which clearly shows the presence of Ti, Fe and O. This is in agreement with the EDS spectrum collected at nanoscale by TEM.

4.6. Raman analysis

In order to identify the structure of the prepared nanocomposites, the sample was analyzed by Raman spectroscopy. The Raman spectrum shows the presence of rutile and unreacted anatase in addition to the modes of pseudobrookite (Fig. 4). The Raman band at 147 cm^{-1} could be attributed to a combination of a B_{1g} mode of rutile and anatase which appear at 143 cm^{-1} and 144 cm^{-1}, respectively and E_g mode of anatase which appears at 147 cm^{-1} [54,55]. The shoulder of the main peak centered at 436 cm^{-1} represents a B_{1g} Raman mode of anatase which appears at 398 cm^{-1} [54,56]. The broad peak centered at 436 cm^{-1} corresponds to a combination of a Raman mode of Fe_2TiO_5 and a E_g mode of rutile which appears at 445 cm^{-1} [55,57]. The XRD pattern is also consistent with the presence of rutile in the composite. However, the anatase phase was not identified by the XRD pattern. The characteristic peak of anatase attributed to the (101) plane appears at 25.25°. However, as identified in the XRD pattern the main intense peak corresponding to the (101) plane of Fe_2TiO_5 appeared at 25.54°. As the 2θ values are similar, it is possible that the observed peak is a combination of both these peaks. Peaks at 199, 222, 334, 436, 658 cm^{-1}, and the broad peak at around 780 cm^{-1} represent the Raman modes of Fe_2TiO_5 [57,58]. Raman spectrum of pure TiO_2 shown in Fig. 4 (b) exhibits four Raman bands at 143, 235, 444, 608 cm^{-1}. Raman bands at 143, 444, 608 cm^{-1} could be attributed to B_{1g}, E_g and A_{1g} characteristic Raman bands of rutile [54] while the broad band at 235 cm^{-1} has risen due to the multiple phonon scattering process [59].

4.7. XPS analysis

The nanocomposites were also characterized by XPS, to determine the elements, chemical bonding and their oxidation state. The survey spectrum (Fig. 5(a)) shows peaks of Fe 2p, Ti 2p, O 1s and C 1s indicating the presence of Fe, Ti, O and C in the prepared nanocomposites. Deconvolution of O 1s high resolution XPS spectrum (Fig. 5(b)) indicates the presence of C═O, C–O and OH which were assigned to the peaks at 529.90 eV, 532.01 eV and 534.26 eV, respectively [60]. Since O is present in the crystal structure of the synthesized nanocomposites, as Ti–O in TiO_2 and Fe–O–Ti of Fe_2TiO_5, such bonding environments could be assigned to the peaks at 529.90 eV and 532.01 eV, respectively [61,62]. The high resolution spectrum of Ti 2p deconvoluted as shown in Fig. 5(c). It clearly shows the spin – orbital splitting of Ti 2p as $2p_{3/2}$ and $2p_{1/2}$. Peaks at 458.50 eV and 464.11 eV, correspond to the $2p_{3/2}$ and $2p_{1/2}$ of Ti^{3+}, respectively. The other peaks at 460.44 eV and 466.01 eV represent the $2p_{3/2}$ and $2p_{1/2}$ of Ti^{4+}, respectively. The shift in the binding energy from the reported values for Ti^{3+} and Ti^{4+} [63,64] might have resulted due to the two different chemical environments which Ti exists, Fe_2TiO_5 and TiO_2. Ratio of Ti^{3+} and Ti^{4+} of Fe_2TiO_5/TiO_2 is 1:2. XPS high resolution spectrum of pure TiO_2 (Fig. 5(d)) shows the peaks at 458.60, 460.40, 464.31, 465.73, and 472.55 eV indicating the presence of both Ti^{3+} and Ti^{4+} in a ratio of 5.5:1. High oxidation state of the same element possess high binding energy. Similar to Ti, the high resolution XPS spectrum of Fe 2p (Fig. 5(e)) also shows four sub peaks, where the peaks at 711.16 eV and 724.61 eV could be attributed to $2p_{3/2}$ and $2p_{1/2}$ of Fe^{3+}, and those at 719.15 eV and 732.39 eV could be assigned to the satellite peaks of $2p_{3/2}$ and $2p_{1/2}$, respectively [65].

4.8. UV–visible spectroscopy

The optical properties of the synthesized nanocomposites were studied by UV–Visible diffuse reflectance spectroscopy (Fig. 6). The optical absorbance was calculated using the Kubelka-Munk function ($\alpha = (1\text{-}R)^2/2R$). Here, α and R are the absorption coefficient and diffuse reflectance coefficient, respectively [66,67]. The optical absorbance of TiO_2 nanoparticles synthesized by sol gel synthesis and annealed at 800 °C is shown in Fig. 6(a). It shows a significant UV light absorption edge at 425 nm. The light adsorption edge has been red shifted to the visible range in the Fe_2TiO_5/TiO_2 heterostructures commencing around 592 nm as shown in the DRS spectrum with four absorption bands centered at about 406 nm, 494 nm, 602 nm and 795 nm (Fig. 6(b)). To determine the band gap of the semiconductors, the Tauc Plots $((F(R) \times h\nu)^n$ vs $h\nu)$ of TiO_2 and Fe_2TiO_5 were constructed. Tauc plot for the direct band gap transition was plotted using $n = 2$ for the above equation, while the Tauc plots were plotted using $n = ½$ to represent the indirect band gap transitions. For direct band gap transition, the plot shows a linear Tauc region just above the absorption edge, while indirect transitions show an indefinite Tauc region in the plots. Plots corresponding to direct transition of TiO_2 and Fe_2TiO_5 are given in Fig. 6 (c) and (d), respectively and plots that indicate indirect transitions are shown in Figure (e) and (f), respectively. Extrapolations of indirect transitions yield small band gap values, 2.77 and 1.53 eV for TiO_2 and Fe_2TiO_5, respectively. The band gap values obtained from the extrapolations of direct transitions plots are 2.96 and 2.02 eV for the above materials, respectively. The resulting band gap of Fe_2TiO_5 from direct transition is slightly lower than that reported [44]. The presence of metallic and non metallic impurities in the final product (Table 2) may exert a significant effect on band gap values due to the oxygen vacancies and lattice disorientations, affecting the electronic transition from the valence band to the conduction band [68]. Further, it has been shown that the presence of SiO_2 and Fe lower the band gap of TiO_2 by shifting the optical absorption to the visible range [69].

$$E_{CB} = X - E^C - 0.5E_g$$

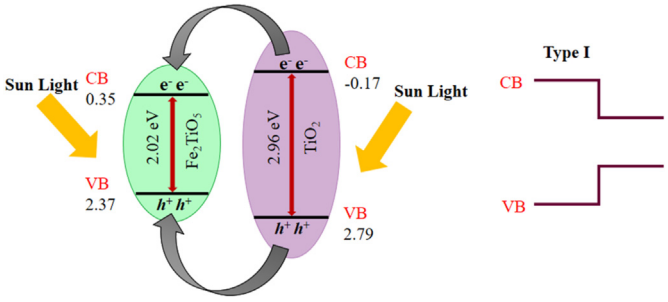

Fig. 7. Representation of valence band (VB) and conduction band (CB) potentials of Fe_2TiO_5, TiO_2 and possible movement of charge carrier in the Fe_2TiO_5/TiO_2 nanocomposite system.

$$E_{VB} = X - E^C + 0.5E_g$$

where X is the electronegativity of the semiconductor determined by the geometric mean of the absolute electronegativity of constituent atoms; E^C is the energy of the free electrons on the hydrogen scale (approximately 4.5 eV); and E_g is the band gap of the semiconductor. The X values for Fe_2TiO_5 and TiO_2 are 5.86 and 5.81 eV, respectively [67]. Based on the above equations E_{CB} values of Fe_2TiO_5 and TiO_2 are estimated to be 0.35 eV and −0.17 eV/normal hydrogen electrode (NHE), respectively. The corresponding E_{VB} values are 2.37 eV and 2.79 eV/NHE, respectively. As depicted by Fig. 7, the CB of Fe_2TiO_5 lies below that of TiO_2 and the VB lies above that of TiO_2 creating a type I band alignment. The photogenerated electrons present in the CB of TiO_2 are transferred to the CB of Fe_2TiO_5, while the holes present in the VB of TiO_2 are also transferred to the VB of Fe_2TiO_5 facilitating the recombination of photogenerated electrons and holes. The hydroxyl radicals and superoxide radicals have been reported as the major reactive species during the photodegradation of organic pollutants by most photocatalytic reactions. These radicals are generated when O_2, H_2O and ^-OH interact with the photogenerated electrons and holes as follows,

$$\text{Photocatalyst} + h\nu = e^- + h^+ \quad (1a)$$

$$O_2 + e^- = O_2^{\bullet-} \quad (2a)$$

$$H_2O + h^+ = {}^{\bullet}OH + H^+ \quad (3a)$$

$$^-OH_{(surface)} + h^+ = {}^{\bullet}OH \quad (4a)$$

The standard redox potentials for $H_2O/{}^{\bullet}OH$, $–OH/{}^{\bullet}OH$ are 2.72 and 1.99 eV vs NHE, respectively [71,72]. The VB potential of Fe_2TiO_5 and TiO_2 are 2.37 and 2.79 eV, respectively. The VB potential of TiO_2 is greater than the redox potential of $H_2O/{}^{\bullet}OH$ and $–OH/{}^{\bullet}OH$, while the VB potential of Fe_2TiO_5 is less than the respective potentials. Hence, the generation of ${}^{\bullet}OH$ by equations (3) and (4) at the VB of TiO_2 is possible, while that at the VB of Fe_2TiO_5 is not possible. The CB potential of both Fe_2TiO_5 (0.35 eV) and TiO_2 (−0.17 eV) are greater than the redox potential for $O_2/O_2^{\bullet-}$ (−0.33 eV vs NHE [71]). Therefore, the generation of $O_2^{\bullet-}$ by equation (2) is not possible at the CB of both Fe_2TiO_5 and TiO_2. In the present study, the photogenerated e^-, h^+ and ${}^{\bullet}OH$ radical jointly participate in degrading the MB dye on illumination with solar light.

4.9. Photocatalytic activity

Photocatalytic activity of Fe_2TiO_5/TiO_2 nanocomposites in degrading MB under natural sunlight was studied where MB was selected as the model compound being a textile dye present in wastewater. Samples were kept in the dark prior to irradiation by sunlight in order to reach the adsorption-desorption equilibrium. The variation of A/A_0 with time of Fe_2TiO_5/TiO_2 and synthesized TiO_2 are shown in Fig. 8 (a) and (b), respectively. It can be clearly seen that the absorption drop of samples incubated with Fe_2TiO_5/TiO_2. This observation could be attributed to the high porosity and high surface area of the synthesized Fe_2TiO_5/TiO_2. As

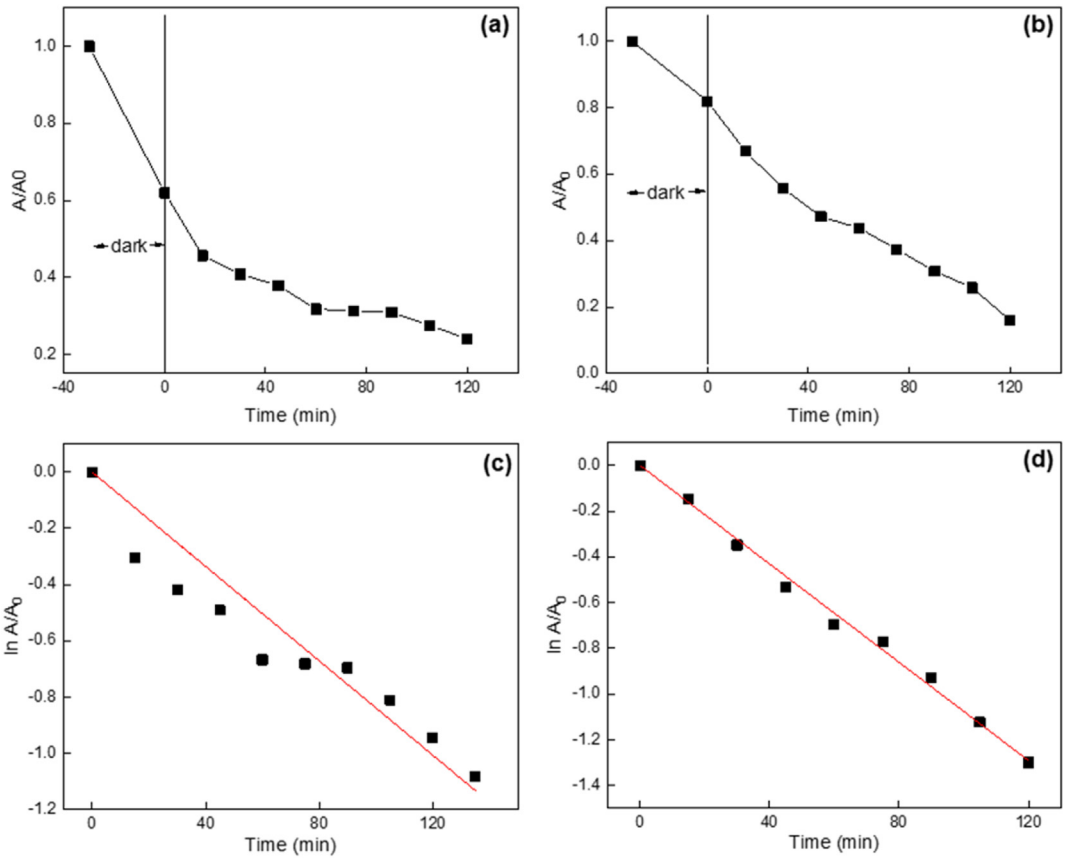

Fig. 8. The absorbance changes of methylene blue dye as a function of irradiation time under solar light of (a) Fe_2TiO_5/TiO_2 (b) TiO_2, Plot of ln A/A_0 vs irradiation time of (c) Fe_2TiO_5/TiO_2 (d) TiO_2. (For interpretation of the references to colour in this figure legend, the reader is referred to the Web version of this article.)

revealed by the TEM and SEM images in Figs. 2 and 3, respectively the surface to volume ratio is high in the synthesized Fe_2TiO_5/TiO_2 nanocomposites. Hence, more MB molecules would be adsorbed to the surface active sites of Fe_2TiO_5/TiO_2. As the MB molecules are positively charged the adsorption sites should to be negatively charged to facilitate a better adsorption. This suggests that the surface of the Fe_2TiO_5/TiO_2 is negatively charged. The larger negative charge could be attributed to the greater presence of surface oxygen in Fe_2TiO_5/TiO_2. Adsorption of the reactant molecules to the catalyst surface promotes the catalytic reaction as the close proximity of the catalyst to the reactant molecules facilitates the electron and radical transfer. Adsorption drop with pure TiO_2 synthesized by sol gel method is lower than that with Fe_2TiO_5/TiO_2 which could be due to the low porosity and surface area. Kinetic plots for the degradation of MB by Fe_2TiO_5/TiO_2 and TiO_2 are shown in Fig. 8 (c) and (d), respectively.

The rate constant for mineralization of MB by Fe_2TiO_5/TiO_2 is 0.0084 min^{-1} and only 75.95% decoloration of MB was observed after 2 h indicating incomplete mineralization. As explained in the XRD analysis the weight ratio of Fe_2TiO_5 to TiO_2 of the synthesized nanohybrid, Fe_2TiO_5/TiO_2 is 5:1. Therefore, it can be concluded that Fe_2TiO_5 alone contributes more to the photocatalytic activity than the Fe_2TiO_5/TiO_2 heterojuction. Electron-hole pair recombination occurs at both Fe_2TiO_5 and the heterojunction resulting in a low photocatalytic activity as shown in Fig. 7. Similarly, photocatalytic activity of pure TiO_2 annealed at 800 °C was also investigated under the same conditions. The rate constant for mineralization of MB by TiO_2 is 0.01076 min^{-1} and 77.87% decoloration of MB was observed after 2 h. Pure TiO_2 has shown a slightly higher photodegradation rate than Fe_2TiO_5/TiO_2. This has resulted because the amount of MB adsorbed to Fe_2TiO_5/TiO_2 under dark conditions is 52% higher than MB adsorbed to pure TiO_2. Reactant species should get adsorbed or at least be in close proximity to the catalyst surface for the catalytic reaction to take place. Therefore, it is suggested that MB adsorbed during the dark conditions is also degraded first upon exposure to sunlight, vacating the catalyst surface for the adsorption of free MB molecules in the solution. Therefore, amount MB molecules degraded during the whole time period by Fe_2TiO_5/TiO_2 is higher than that by TiO_2. When the first hour of the catalyst being exposed to MB molecules is considered, including the 30 min which they were kept is dark, the rate constant for the MB degradation by Fe_2TiO_5/TiO_2 and TiO_2 are 0.01027 and 0.00746 min^{-1}, respectively. This clearly shows that photocatalytic activity of Fe_2TiO_5/TiO_2 is greater than that of pure TiO_2. Further, as revealed by the XPS analysis pure TiO_2 contains both Ti^{3+} and Ti^{4+} in a ratio of 5.5:1 at the surface, while that of Fe_2TiO_5/TiO_2 is 1:2. Ti^{3+} and oxygen vacancies are known to enhance visible light absorption [73]. The existence of the defect states just below and its overlap with the conduction band could explain the enhanced photocatalytic properties of the self-doped TiO_2 [74]. Hence as pure TiO_2 contains more Ti^{3+} that has also contributed to considerable photocatalytic activity.

As revealed by the XRF analysis Fe_2TiO_5/TiO_2 consists of many other metal and non-metal species. These impurities lower the band gap and facilitate electron transfer to the MB molecules. Incorporation of SiO_2 to TiO_2 has been found to enhance the photocatalytic activity of TiO_2. However, the photocatalytic activity of TiO_2 decreased with high ratios of SiO_2:TiO_2 [75]. TiO_2 modified with Fe^{3+} has also shown improved photocatalytic activity when loaded on Al_2O_3 [76]. Further, Al_2O_3 doped Mn_3O_4 nanomaterials have exhibited high solar photocatalytic activity [77]. Another study indicates that the photocatalytic activity of TiO_2 is inhibited by MnO_2 at lower concentrations due to the formation of heterojunctions between MnO_2 and TiO_2 particles. Further, MnO_2 in contact with TiO_2 broaden the band gap, reducing the absorption of UV radiation. It can also create impurity levels serving as photogenerated electron-hole pair recombination centers, triggering the electron-hole

pair recombination [78]. However, it has been reported that only MnO_2 is a low cost, highly effective photocatalyst with a band gap of 1–2 eV which could be driven by visible light [79]. Further, the findings indicate that MnO_2 coupled with TiO_2 produces high photocatalytic activity as the presence of TiO_2 minimizes electron-hole pair recombination and slow charge transfer in MnO_2. The visible light sensitivity of the photocatalytic activity of TiO_2 improved due to the presence of MnO_2 [79]. Cr_2O_3–TiO_2 mixed oxides [80], Cr_2O_3/Carbon nanotube/TiO_2 composite materials [81] have shown increased visible light absorption, allowing greater applicability. Therefore, it is evident that impurities present in Fe_2TiO_5/TiO_2 have an effect on photocatalytic activity. The observed catalytic activity suggests that it may be possible to use the synthesized photocatalysts to degrade other toxic organic pollutants.

5. Conclusions

In summary, we have synthesized Fe_2TiO_5/TiO_2 binary nanocomposites by bottom up approaches using natural ilmenite sand. The type of heterostructure plays a crucial role in photocatalytic activity. Electron-hole pair recombination was facilitated by the type I band alignment due to the accumulation of electrons in the conduction band and holes in the valence band of Fe_2TiO_5. We believe that this new input directs the design and synthesis of new photocatalytic systems that could be used to produce a cleaner environment.

Data accessibility

The datasets supporting this article have been included in the main text and in the supplementary information.

CrediT author statement

Charitha Thambiliyagodage conceived the idea, designed the project, performed some experiments, acquired funds, supervise the students, interpreted the data, wrote the first draft of the manuscript and edited the manuscript with Ramanee Wijesekara and Martin Bakker. Shanitha Mirihana performed the major part of the experiments. Ramanne Wijesekara contributed immensely on editing the manuscript. Dinu Siri Madusanka and Murthi Kandanapitiye performed some experiments. Ramanne Wijesekara, Murthi Kandanapitiye and Martin Bakker contributed to acquire funds. All authors of this paper have read and approved the final version submitted.

Funding statement

This research was supported by the Accelerating Higher Education Expansion and Development (AHEAD) Operation of the Ministry of Higher Education funded by the World Bank.

Declaration of competing interest

The authors declare that they have no known competing financial interests or personal relationships that could have appeared to influence the work reported in this paper.

Acknowledgement

Authors acknowledge Sri Lanka Institute of Nanotechnology for providing the instrument facilities.

References

[1] F. Fu, Q. Wang, Removal of heavy metal ions from wastewaters: a review, J. Environ. Manag. (2011), https://doi.org/10.1016/j.jenvman.2010.11.011.
[2] N.M. Mahmoodi, B. Hayati, M. Arami, C. Lan, Adsorption of textile dyes on Pine Cone from colored wastewater: kinetic, equilibrium and thermodynamic studies, Desalination 268 (1–3) (Mar. 2011) 117–125, https://doi.org/10.1016/j.desal.2010.10.007.
[3] I. Oller, S. Malato, J.A. Sánchez-Pérez, M.I. Maldonado, R. Gassó, Detoxification of wastewater containing five common pesticides by solar AOPs-biological coupled system, Catal. Today 129 (1–2) (Nov. 2007) 69–78, https://doi.org/10.1016/j.cattod.2007.06.055. SPEC.
[4] G. El Diwani, S. El Rafie, N.N. El Ibiari, H.I. El-Aila, Recovery of ammonia nitrogen from industrial wastewater treatment as struvite slow releasing fertilizer, Desalination 214 (1–3) (Aug. 2007) 200–214, https://doi.org/10.1016/j.desal.2006.08.019.
[5] A. Nikolaou, S. Meric, D. Fatta, Occurrence patterns of pharmaceuticals in water and wastewater environments, in *Analytical and Bioanalytical Chemistry*, Feb. 387 (4) (2007) 1225–1234, https://doi.org/10.1007/s00216-006-1035-8.
[6] Ihsanullah, et al., Heavy metal removal from aqueous solution by advanced carbon nanotubes: critical review of adsorption applications, Separ. Purif. Technol. 157 (Jan. 2016) 141–161, https://doi.org/10.1016/J.SEPPUR.2015.11.039.
[7] T.R. Harper, N.W. Kingham, Removal of arsenic from wastewater using chemical precipitation methods, Water Environ. Res. 64 (3) (May 1992) 200–203, https://doi.org/10.2175/WER.64.3.2.
[8] Y. Al-Degs, M.A.M. Khraisheh, S.J. Allen, M.N. Ahmad, Effect of carbon surface chemistry on the removal of reactive dyes from textile effluent, Water Res. 34 (3) (Feb. 2000) 927–935, https://doi.org/10.1016/S0043-1354(99)00200-6.
[9] A.I. Zouboulis, N.K. Lazaridis, A. Grohmann, Toxic metals removal from waste waters by upflow filtration with floating filter medium. I. The case of zinc, Separ. Sci. Technol. 37 (2) (Nov 2002) 403–416, https://doi.org/10.1081/SS-120000795.
[10] R. Eliassen and G. E. Bennett, "Anion exchange and filtration techniques for wastewater renovation," Journal (Water Pollution Control Federation), vol. 39. doi: 10.2307/25035847.
[11] E. H. Snider and J. J. Porter, "Ozone treatment of dye waste," Journal (Water Pollution Control Federation), vol. 46. pp. 886–894, doi: 10.2307/25038731.
[12] L. Szpyrkowicz, J. Naumczyk, F. Zilio-Grandi, Electrochemical treatment of tannery wastewater using TiPt and Ti/Pt/Ir electrodes, Water Res. 29 (2) (Feb. 1995) 517–524, https://doi.org/10.1016/0043-1354(94)00176-8.
[13] J. Saien, F. Shahrezaei, Organic pollutants removal from petroleum refinery wastewater with nanotitania photocatalyst and UV light emission, Int. J. Photoenergy (2012), https://doi.org/10.1155/2012/703074, 1–5, Jan. 2012.
[14] R. S. Dariani, A. Esmaeili, A. Mortezaali, and S. Dehghanpour, "Photocatalytic reaction and degradation of methylene blue on TiO2 nano-sized particles," Optik, vol. 127, no. 18, pp. 7143–7154, Sep. 2016, doi: 10.1016/J.IJLEO.2016.04.026.
[15] S. Chakrabarti, B.K. Dutta, Photocatalytic degradation of model textile dyes in wastewater using ZnO as semiconductor catalyst, J. Hazard Mater. 112 (3) (Aug. 2004) 269–278, https://doi.org/10.1016/J.JHAZMAT.2004.05.013.
[16] S.-W. C, Y.-J. Zhu*, Hierarchically Nanostructured α-Fe2O3 Hollow Spheres: Preparation, Growth Mechanism, Photocatalytic Property, and Application in Water Treatment, 2008, https://doi.org/10.1021/JP8000465.
[17] T.L. Thompson, J.T. Yates, Surface science studies of the photoactivation of TIO2 - new photochemical processes, Chem. Rev. 106 (10) (Oct. 2006) 4428–4453, https://doi.org/10.1021/cr050172k. American Chemical Society.
[18] K. Sivula, F. LeFormal, M. Grätzel, Solar water splitting: progress using hematite (α-Fe2O3) photoelectrodes, ChemSusChem 4 (4) (Apr. 2011) 432–449, https://doi.org/10.1002/cssc.201000416.
[19] D.H. Kim, H.S. Hong, S.J. Kim, J.S. Song, K.S. Lee, Photocatalytic behaviors and structural characterization of nanocrystalline Fe-doped TiO2 synthesized by mechanical alloying, J. Alloys Compd. 375 (1–2) (Jul. 2004) 259–264, https://doi.org/10.1016/j.jallcom.2003.11.044.
[20] G. Colón, M. Maicu, M.C. Hidalgo, J.A. Navío, Cu-doped TiO2 systems with improved photocatalytic activity, Appl. Catal. B Environ. 67 (1–2) (Sep. 2006) 41–51, https://doi.org/10.1016/j.apcatb.2006.03.019.
[21] M.A. Barakat, R.I. Al-Hutailah, E. Qayyum, J. Rashid, J.N. Kuhn, Pt nanoparticles/TiO $_2$ for photocatalytic degradation of phenols in wastewater, Environ. Technol. 35 (2) (Jan. 2014) 137–144, https://doi.org/10.1080/09593330.2013.820796.
[22] S.A. Ansari, M.M. Khan, M.O. Ansari, M.H. Cho, Nitrogen-doped titanium dioxide (N-doped TiO2) for visible light photocatalysis, New J. Chem. 40 (4) (Apr. 01, 2016) 3000–3009, https://doi.org/10.1039/c5nj03478g. Royal Society of Chemistry.
[23] F. Dong, S. Guo, H. Wang, X. Li, Z. Wu, Enhancement of the visible light photocatalytic activity of C-doped Tio2 nanomaterials prepared by a green synthetic approach, J. Phys. Chem. C 115 (27) (Jul. 2011) 13285–13292, https://doi.org/10.1021/jp111916q.
[24] T. Umebayashi, T. Yamaki, S. Tanaka, K. Asai, Visible light-induced degradation of methylene blue on S-doped TiO2, Chem. Lett. 32 (4) (Apr. 2003) 330–331, https://doi.org/10.1246/cl.2003.330.
[25] Y. Cai, et al., Hydrothermal-ultrasonic synthesis of CuO nanorods and CuWO4 nanoparticles for catalytic reduction, photocatalysis activity, and antibacterial properties, Mater. Chem. Phys. 258 (Jan. 2021) 123919, https://doi.org/10.1016/j.matchemphys.2020.123919.
[26] C. Zhao, et al., One step and fast preparation of VOx/g-C3N4 photocatalyst via microwave heating for effective degradation of RhB under visible light, J. Phys. Chem. Solid. 136 (Jan. 2020) 109122, https://doi.org/10.1016/j.jpcs.2019.109122.
[27] P. Chen, et al., Microwave heating preparation of phosphorus doped g-C3N4 and its enhanced performance for photocatalytic H2 evolution in the help of Ag3PO4 nanoparticles, Int. J. Hydrogen Energy 45 (28) (May 2020) 14354–14367, https://doi.org/10.1016/j.ijhydene.2020.03.169.
[28] J. Wen, X. Liu, L. Liu, X. Ma, A. Fakhri, V.K. Gupta, Bimetal cobalt-Iron based organic frameworks with coordinated sites as synergistic catalyst for fenton

catalysis study and antibacterial efficiency, Colloids Surfaces A Physicochem. Eng. Asp. 610 (Feb. 2021) 125683, https://doi.org/10.1016/j.colsurfa.2020.125683.
[29] M. Yang, et al., Biosynthesis of nano bimetallic Ag/Pt alloy from Crocus sativus L. extract: biological efficacy and catalytic activity, J. Photochem. Photobiol. B Biol. 212 (Nov. 2020) 112025, https://doi.org/10.1016/j.jphotobiol.2020.112025.
[30] B. Liu, et al., CaIn 2 S 4 decorated WS 2 hybrid for efficient Cr(VI) reduction, Appl. Surf. Sci. 484 (Aug. 2019) 300–306, https://doi.org/10.1016/j.apsusc.2019.03.322.
[31] X. Liu, et al., Cu2In2ZnS5/Gd2O2S:Tb for full solar spectrum photoreduction of Cr(VI) and CO2 from UV/vis to near-infrared light, Appl. Catal. B Environ. 249 (Jul. 2019) 82–90, https://doi.org/10.1016/j.apcatb.2019.02.061.
[32] B. Liu, et al., Efficient charge separation between UiO-66 and ZnIn2S4 flowerlike 3D microspheres for photoelectronchemical properties, Appl. Catal. B Environ. 226 (Jun. 2018) 234–241, https://doi.org/10.1016/j.apcatb.2017.12.052.
[33] Z. Ren, X. Liu, Z. Zhuge, Y. Gong, C.Q. Sun, MoSe2/ZnO/ZnSe hybrids for efficient Cr(VI) reduction under visible light irradiation, Chin. J. Catal. 41 (1) (Jan. 2020) 180–187, https://doi.org/10.1016/S1872-2067(19)63484-4.
[34] K. Cui, et al., Effects of Cr2O3 content on microstructure and mechanical properties of Al2O3 matrix composites, Coatings 2021 11 (2) (Feb. 2021) 234, https://doi.org/10.3390/COATINGS11020234. Page 234, vol. 11.
[35] Y. Zhang, et al., Evolution of surface morphology, roughness and texture of tungsten disilicide coatings on tungsten substrate, Vacuum 191 (Sep. 2021) 110297, https://doi.org/10.1016/J.VACUUM.2021.110297.
[36] Y. Zhang, et al., "Formation of MoSi2 and Si/MoSi2 coatings on TZM (Mo–0.5Ti–0.1Zr–0.02C) alloy by hot dip silicon-plating method, Ceram. Int. 47 (16) (Aug. 2021) 23053–23065, https://doi.org/10.1016/J.CERAMINT.2021.05.020.
[37] F.A. Morsy, S. El-Sherbiny, M. Samir, O.A. Fouad, Application of nanostructured titanium dioxide pigments in paper coating: a comparison between prepared and commercially available ones, J. Coating Technol. Res. 13 (2) (Mar. 2016) 307–316, https://doi.org/10.1007/s11998-015-9735-7.
[38] " Attributes, Characteristics, and applications of titanium and its alloys. https://www.tms.org/pubs/journals/JOM/1005/boyer-1005.html, Mar. 23, 2020.
[39] M. Ramezani, A. Davoodi, A. Malekizad, S.M. Hosseinpour-Mashkani, "Synthesis and characterization of Fe2TiO5 nanoparticles through a sol–gel method and its photocatalyst applications, J. Mater. Sci. Mater. Electron. 26 (6) (Jun. 2015) 3957–3962, https://doi.org/10.1007/s10854-015-2930-6.
[40] Y. Zhang, W. Lv, X. Lv, C. Bai, K. Han, B. Song, Oxidation kinetics of ilmenite concentrate by non-isothermal thermogravimetric analysis, 24, J. Iron Steel Res. Int. 247 (7) (2017) 678–684, https://doi.org/10.1016/S1006-706X(17)30102-4. Jul. 2017.
[41] Y. Zhang, et al., "Isothermal reduction kinetics of Panzhihua ilmenite concentrate under 30vol% CO–70vol% N 2 atmosphere, 24, Int. J. Miner. Metall. Mater. 243 (3) (2017) 240–248, https://doi.org/10.1007/S12613-017-1401-X. Mar. 2017.
[42] Y. Zhang, J. Zhao, X. Ma, M. Li, Y. Lv, X. Gao, "Isothermal reduction kinetics and mechanism of pre-oxidized ilmenite," *mining*, 36, Metall. Explor. 364 (4) (2019) 825–837, https://doi.org/10.1007/S42461-019-0075-5. May 2019.
[43] M. Waqas, et al., Multi-shelled TiO2/Fe2TiO5 heterostructured hollow microspheres for enhanced solar water oxidation, Nano Res. 10 (11) (Nov. 2017) 3920–3928, https://doi.org/10.1007/s12274-017-1606-3.
[44] Q. Liu, et al., Aligned Fe2 TiO5-containing nanotube arrays with low onset potential for visible-light water oxidation, Nat. Commun. 5 (1) (Oct. 2014) 1–7, https://doi.org/10.1038/ncomms6122.
[45] K.M. Min, K.S. Park, A.H. Lim, J.C. Kim, D.W. Kim, Synthesis of pseudobrookite-type Fe 2TiO 5 nanoparticles and their Li-ion electroactivity, Ceram. Int. 38 (7) (Sep. 2012) 6009–6013, https://doi.org/10.1016/j.ceramint.2012.03.044.
[46] F. Liu, H. He, C. Zhang, Novel iron titanate catalyst for the selective catalytic reduction of NO with NH3 in the medium temperature range, Chem. Commun. 17 (Apr. 2008) 2043–2045, https://doi.org/10.1039/b800143j.
[47] K. Hooshyari, M. Javanbakht, L. Naji, M. Enhessari, Nanocomposite proton exchange membranes based on Nafion containing Fe2TiO5 nanoparticles in water and alcohol environments for PEMFC, J. Membr. Sci. 454 (Mar. 2014) 74–81, https://doi.org/10.1016/j.memsci.2013.11.033.
[48] Z. Lou, Y. Li, H. Song, Z. Ye, L. Zhu, Fabrication of Fe2TiO5/TiO2 nanoheterostructures with enhanced visible-light photocatalytic activity, RSC Adv. 6 (51) (May 2016) 45343–45348, https://doi.org/10.1039/c6ra06763h.
[49] T.P.B. Rajakaruna, C.P. Udawatte, R. Chandrajith, R.M.G. Rajapakse, Nonhazardous process for extracting pure titanium dioxide nanorods from geogenic ilmenite, ACS Omega 5 (26) (Jul. 2020) 16176–16182, https://doi.org/10.1021/ACSOMEGA.0C01756.
[50] W. Li, T. Zeng, Preparation of TiO2 anatase nanocrystals by TiCl4 hydrolysis with additive H2SO4, PloS One 6 (6) (2011), e21082, https://doi.org/10.1371/JOURNAL.PONE.0021082.
[51] S. Wahyuningsih, et al., Decomposition of ilmenite in hydrochloric acid to obtain high grade titanium dioxide, Asian J. Chem. 25 (12) (2013) 6791–6794, https://doi.org/10.14233/AJCHEM.2013.14692.
[52] R.A. Spurr, H. Myers, Quantitative analysis of anatase-rutile mixtures with an X-ray diffractometer, Anal. Chem. 29 (5) (1957) 760–762, https://doi.org/10.1021/ac60125a006.
[53] X.M. Gao, M.W. Li, Y.L. Hou, C.Y. Wang, Characterisation of Fe2TiO5 nanocrystallites synthesised via homogeneous precipitation, Mater. Res. Innovat. 19 (1) (Jan. 2015) 1–6, https://doi.org/10.1179/1433075X13Y.0000000195.
[54] V. Tamilselvan, D. Yuvaraj, R. Rakesh Kumar, K. Narasimha Rao, Growth of rutile TiO 2 nanorods on TiO 2 seed layer deposited by electron beam evaporation, Appl. Surf. Sci. 258 (10) (Mar. 2012) 4283–4287, https://doi.org/10.1016/j.apsusc.2011.12.079.
[55] A. Wypych, et al., Dielectric properties and characterisation of titanium dioxide obtained by different chemistry methods, J. Nanomater. (2014) 124814, https://doi.org/10.1155/2014/124814, 2014.
[56] Z. Zhao, B.K. Tay, G. Yu, Room-temperature deposition of amorphous titanium dioxide thin film with high refractive index by a filtered cathodic vacuum arc technique, Appl. Opt. 43 (6) (Feb. 2004) 1281–1285, https://doi.org/10.1364/AO.43.001281.
[57] M.V. Nikolic, et al., Humidity sensing properties of nanocrystalline pseudobrookite (Fe2TiO5) based thick films, Sensor. Actuator. B Chem. 277 (Dec. 2018) 654–664, https://doi.org/10.1016/j.snb.2018.09.063.
[58] D. Bersani, P.P. Lottici, A. Montenero, Micro-Raman study of iron-titanium oxides obtained by sol-gel synthesis, J. Mater. Sci. 35 (17) (Sep. 2000) 4301–4305, https://doi.org/10.1023/A:1004884302755.
[59] H.L. Ma, J.Y. Yang, Y. Dai, Y.B. Zhang, B. Lu, G.H. Ma, Raman study of phase transformation of TiO 2 rutile single crystal irradiated by infrared femtosecond laser, Appl. Surf. Sci. 253 (18) (Jul. 2007) 7497–7500, https://doi.org/10.1016/j.apsusc.2007.03.047.
[60] M. Smith, L. Scudiero, J. Espinal, J.S. McEwen, M. Garcia-Perez, Improving the deconvolution and interpretation of XPS spectra from chars by ab initio calculations, Carbon N. Y. 110 (Dec. 2016) 155–171, https://doi.org/10.1016/j.carbon.2016.09.012.
[61] S. Guo, S. Wang, N. Wu, J. Liu, Y. Ni, W. Liu, Facile synthesis of porous Fe2TiO5 microparticulates serving as anode material with enhanced electrochemical performances, RSC Adv. 5 (126) (Nov. 2015) 103767–103775, https://doi.org/10.1039/c5ra22930h.
[62] B. Erdem, R.A. Hunsicker, G.W. Simmons, E. David Sudol, V.L. Dimonie, M.S. El-Aasser, XPS and FTIR surface characterization of TiO2 particles used in polymer encapsulation, Langmuir 17 (9) (May 2001) 2664–2669, https://doi.org/10.1021/la0015213.
[63] V.V. Atuchin, V.G. Kesler, N.V. Pervukhina, Z. Zhang, Ti 2p and O 1s core levels and chemical bonding in titanium-bearing oxides, J. Electron. Spectrosc. Relat. Phenom. 152 (1–2) (Jun. 2006) 18–24, https://doi.org/10.1016/j.elspec.2006.02.004.
[64] F. Guillemot, M.C. Porté, C. Labrugère, C. Baquey, Ti4+ to Ti3+ conversion of TiO2 uppermost layer by low-temperature vacuum annealing: interest for titanium biomedical applications, J. Colloid Interface Sci. 255 (1) (Nov. 2002) 75–78, https://doi.org/10.1006/jcis.2002.8623.
[65] M.C. Biesinger, B.P. Payne, A.P. Grosvenor, L.W.M. Lau, A.R. Gerson, R.S.C. Smart, Resolving surface chemical states in XPS analysis of first row transition metals, oxides and hydroxides: Cr, Mn, Fe, Co and Ni, Appl. Surf. Sci. 257 (7) (Jan. 2011) 2717–2730, https://doi.org/10.1016/j.apsusc.2010.10.051.
[66] Q. Li, R. Xie, W.L. Yin, E.A. Mintz, K.S. Jian, Enhanced visible-light-induced photocatalytic disinfection of E. coli by carbon-sensitized nitrogen-doped titanium oxide, Environ. Sci. Technol. 41 (14) (Jul. 2007) 5050–5056, https://doi.org/10.1021/es062753c.
[67] K. Xiong, et al., Heterostructured ZnFe2O4/Fe2TiO5/TiO2 composite nanotube Arrays with an improved photocatalysis degradation efficiency under simulated sunlight irradiation, Nano-Micro Lett. 10 (1) (Jan. 2018), https://doi.org/10.1007/s40820-017-0169-x.
[68] E.M. Samsudin, S.B. Abd Hamid, Effect of band gap engineering in anionic-doped TiO 2 photocatalyst, Appl. Surf. Sci. 391 (Jan. 2017) 326–336, https://doi.org/10.1016/j.apsusc.2016.07.007.
[69] M. Karbassi, A. Nemati, M.H. Zari, K. Ahadi, Effect of iron oxide and silica doping on microstructure, bandgap and photocatalytic properties of titania by water-in-oil microemulsion technique, Trans. Indian Ceram. Soc. 70 (4) (Oct. 2011) 227–232, https://doi.org/10.1080/0371750X.2011.10600173.
[70] X. Guan, L. Guo, Cocatalytic Effect of SrTiO3 on Ag3PO4 toward enhanced photocatalytic water oxidation, ACS Catal. 4 (9) (Sep. 2014) 3020–3026, https://doi.org/10.1021/cs5005079.
[71] D. Majhi, K. Das, A. Mishra, R. Dhiman, B.G. Mishra, One pot synthesis of CdS/BiOBr/Bi2O2CO3: a novel ternary double Z-scheme heterostructure photocatalyst for efficient degradation of atrazine, Appl. Catal. B Environ. 260 (Jan. 2020) 118222, https://doi.org/10.1016/j.apcatb.2019.118222.
[72] Q.A. Drmosh, A. Hezam, A.H.Y. Hendi, M. Qamar, Z.H. Yamani, K. Byrappa, Ternary Bi2S3/MoS2/TiO2 with double Z-scheme configuration as high performance photocatalyst, Appl. Surf. Sci. 499 (Jan. 2020) 143938, https://doi.org/10.1016/j.apsusc.2019.143938.
[73] M. Xing, W. Fang, M. Nasir, Y. Ma, J. Zhang, M. Anpo, Self-doped Ti3+-enhanced TiO2 nanoparticles with a high-performance photocatalysis, J. Catal. 297 (Jan. 2013) 236–243, https://doi.org/10.1016/j.jcat.2012.10.014.
[74] I. Justicia, et al., Designed self-doped titanium oxide thin films for efficient visible-light photocatalysis, Adv. Mater. 14 (19) (Oct. 2002) 1399–1402, https://doi.org/10.1002/1521-4095(20021002)14:19<1399::AID-ADMA1399>3.0.CO;2-C.
[75] C. Anderson, A.J. Bard, Improved photocatalyst of TiO2/SiO2 prepared by a sol-gel synthesis, J. Phys. Chem. 99 (24) (1995) 9882–9885, https://doi.org/10.1021/j100024a033.
[76] J. Pei, W. Ma, R. Li, Y. Li, H. Du, Preparation and photocatalytic properties of TiO2-Al2O3 composite loaded catalysts, J. Chem. 2015 (2015), https://doi.org/10.1155/2015/806568.
[77] S.A. Bin Asif, S.B. Khan, A.M. Asiri, Visible light functioning photocatalyst based on Al2O3 doped Mn3O4 nanomaterial for the degradation of organic toxin, Nanoscale Res. Lett. 10 (1) (Dec. 2015) 1–10, https://doi.org/10.1186/s11671-015-0990-4.
[78] S. Li, Z. Ma, L. Wang, J. Liu, Influence of MnO2 on the photocatalytic activity of P-25 TiO2 in the degradation of methyl orange, Sci. China, Ser. B Chem. 51 (2) (Feb. 2008) 179–185, https://doi.org/10.1007/s11426-007-0100-2.
[79] S.L. Chiam, S.Y. Pung, F.Y. Yeoh, Recent developments in MnO2-based photocatalysts for organic dye removal: a review, Environ. Sci. Pollut. Control Ser.

27 (6) (Feb. 01, 2020) 5759–5778, https://doi.org/10.1007/s11356-019-07568-8. Springer.

[80] Y.S. Jung, K.H. Kim, T.Y. Jang, Y. Tak, S.H. Baeck, Enhancement of photocatalytic properties of Cr2O 3-TiO2 mixed oxides prepared by sol-gel method, Curr. Appl. Phys. 11 (3) (May 2011) 358–361, https://doi.org/10.1016/j.cap.2010.08.001.

[81] M.L. Chen, K.Y. Cho, W.C. Oh, Synthesis and photocatalytic behaviors of Cr2O 3-CNT/TiO2 composite materials under visible light, J. Mater. Sci. 45 (24) (Dec. 2010) 6611–6616, https://doi.org/10.1007/s10853-010-4751-6.